ACS OMEGA

Open Access

http://pubs.acs.org/journal/acsodf

Article

Synergistic Effect of Group 9 Metals on the Performance of Hydrotalcite-Derived Ni Catalysts for Methane Dry Reforming

Sumia Manzoor,[#] Ahmed Abotaleb,[#] Nada Abounahia, Yongfeng Tong, Ivan Gladich, Abdraman Moussa, Mohammed Alshamari, Abdulrahman Altay, Tareq Al-Ansari,[*] and Alessandro Sinopoli[*]

Cite This: https://doi.org/10.1021/acsomega.5c08293

Read Online

ACCESS | Metrics & More | Article Recommendations | Supporting Information

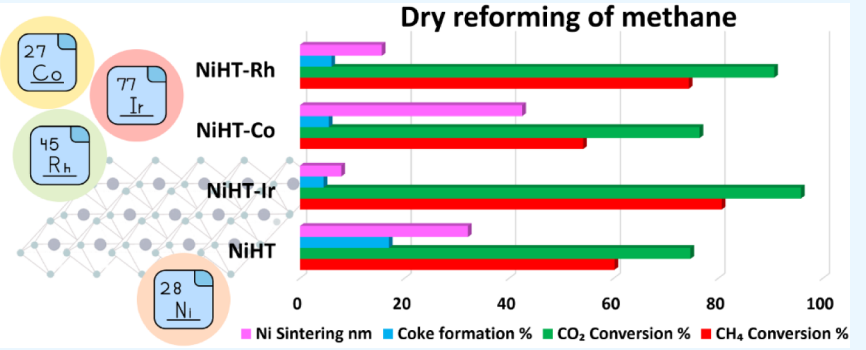

ABSTRACT: Dry reforming of methane (DRM) offers an efficient pathway for the simultaneous utilization of CO_2 and CH_4, two of the most impactful greenhouse gases, through their conversion into valuable synthesis gas. Nevertheless, the practical deployment of DRM remains challenged by catalyst deactivation, predominantly caused by carbon accumulation and metal sintering. In this work, we explore the impact of group 9 metal promoters, specifically iridium (Ir), cobalt (Co), and rhodium (Rh), on the catalytic behavior and stability of nickel-based materials derived from hydrotalcite precursors. The catalysts were synthesized via a coprecipitation method and thoroughly characterized using a combination of structural, morphological, and surface analytical techniques, alongside hydrogen temperature-programmed reduction (H_2-TPR) and temperature-programmed desorption analyses for CO_2 (CO_2-TPD) and NH_3 (NH_3-TPD). Catalytic testing was conducted at 750 °C over a 20-h period. The addition of Ir and Rh was found to markedly enhance Ni dispersion, strengthen metal−support interactions, and increase the abundance of strong basic sites, all contributing to reduced carbon formation. Among the catalysts, NiHT-Ir demonstrated the highest stability and activity, maintaining CH_4 and CO_2 conversions above 80% with minimal deactivation. NiHT-Rh similarly exhibited excellent catalytic performance and coke resistance. By contrast, NiHT-Co showed a decline in performance associated with severe Ni sintering, while the monometallic NiHT catalyst suffered rapid deactivation. Post-reaction analyses confirmed that Ir and Rh effectively limited coke deposition and metal aggregation, whereas Co promoted Ni particle growth. Density functional theory (DFT) calculations were carried out to elucidate the variations in adsorption behavior of CH_4 and CO_2 across the different catalyst surfaces. This study underscores the beneficial role of group 9 metals, particularly Ir and Rh, in enhancing the catalytic efficiency, stability, and resistance to the deactivation of hydrotalcite-derived Ni-based catalysts for DRM.

1. INTRODUCTION

Methane and carbon dioxide are two of the most significant contributors to global warming and climate change. Methane, in particular, is a highly potent greenhouse gas with a global warming potential approximately 27 times greater than that of CO_2 over a 100-year period.[1] Human activities, largely influenced by industrialization and continued reliance on fossil fuels, are responsible for nearly 30% of the current global temperature rise attributed to methane emissions. As the primary component of natural gas, methane is predominantly released through fossil fuel extraction and distribution, along with emissions from agriculture and waste management. Reducing methane emissions is therefore considered one of the most effective and immediate strategies to slow the pace of climate change while advancing low-carbon energy systems. In this context, dry reforming of methane (DRM) offers a

Received: August 17, 2025
Revised: September 21, 2025
Accepted: September 24, 2025

promising solution by simultaneously utilizing CH_4 and CO_2 to produce synthesis gas, a valuable feedstock for synthetic fuels and various industrial chemicals. In addition, other potential benefits of DRM include valorizing natural gas fields with high amounts of CO_2 and exothermic−endothermic recycling systems for the transport and storage of energy using waste heat from highly exothermic processes, mainly renewable or nuclear energy. While DRM reduces GHG emissions from the environment, the energy-intensive nature presents many challenges, among which the effectiveness of this process is mainly influenced by the catalysts employed. The primary obstacles that dry reforming of methane catalysts encounter are coking due to carbon poisoning and sintering of the active phase, which are both detrimental to the catalyst's performance.[2] These issues result in the catalyst becoming deactivated. Additionally, DRM catalysts often struggle with low activity and selectivity.[3] Improving the catalytic performance is consequently a significant challenge. One of the main difficulties in DRM is activating both CO_2 and CH_4 reactants, as it is essential for achieving high conversion rates. Furthermore, designing an economically viable catalyst that does not suffer from coking and sintering remains a major obstacle to the industrialization of DRM.[2]

Several investigations have been dedicated in recent years to develop an effective catalyst to improve the DRM performance. Although noble-metal-based catalysts such as Rh, Pt, Pd, Ru, and Ir have shown incredible results, including lower coking tendency, higher activity, and greater resistance to sintering, their costs and limited availability make them neither viable nor sustainable from an industrial perspective. As a result, a commonly investigated alternative to noble metals is nickel-based catalysts due to their abundance, cost-effectiveness, and comparable activity to other noble metals. However, Ni-based catalysts are also prone to carbon deposition and sintering at elevated temperatures.[4,5] Furthermore, the choice of support materials also plays a crucial role in the performance of catalysts, with irreducible oxides like La_2O_3, MgO, and Al_2O_3 showing improved performance compared to reducible oxides.[6] Therefore, efforts to improve Ni-based catalysts, such as adding promoters or designing special structures, are being made with an aim to mitigate these drawbacks and enhance their performance and stability.[7]

Among the widely studied supports for Ni-based catalysts, hydrotalcite-like structures are catching the attention of researchers. Hydrotalcites, also termed layered double hydroxides (LDHs), are composed of positively charged brucite-like layers intercalated with anions and water molecules. Their general formula is expressed as $[M^{2+}_{1-x}M^{3+}_{x}(OH)_2]^{x+}(A^{n-})_{x/n}\cdot mH_2O$, with M^{2+} and M^{3+} representing divalent and trivalent metal cations, respectively, whereas A^{n-} represents the interlayer anions required to balance the positive charge, along with associated water molecules. The chemical composition of the brucite-like layers can be readily modified by substituting different cations, such as Mg^{2+} or Ni^{2+}, thereby tailoring the material's properties. Owing to their structure, hydrotalcites offer a highly adaptable support matrix that can be engineered to optimize metal−support interactions, a critical factor in enhancing catalytic performance.[8] Upon thermal decomposition, they yield homogeneous mixed metal oxides featuring small crystallite sizes, high surface areas, and excellent thermal stability. Especially, when it comes to the stabilization of Ni, the flexible structure allows Ni^{2+} or other transition metals to insert in the brucite layer and incorporate effectively with the formed mixed metal oxides, resulting in small metal particles that are strongly interacted and enhanced nickel dispersion.[5,8] Moreover, the resulting mixed metal oxides retain strong basic properties, enhancing the catalyst's coking resistance. Notably, due to their flexibility, hydrotalcite-derived catalysts can be effectively customized by incorporating additional metals as promoters or secondary active components to further improve catalyst stability.[5,9,10] Furthermore, incorporation of small amounts of noble metals into Ni-based catalysts has shown promise in improving the dispersion of active species and enhancing resistance to carbon deposition, offering a potential compromise between performance and cost.[11]

Incorporating group 9 elements, iridium (Ir), rhodium (Rh), and cobalt (Co), into hydrotalcite-based catalysts provides a range of advantages that significantly enhance their performance, particularly in DRM.[5,8,12,13] Iridium, in particular, has a high Tammann temperature, which plays a crucial role in increasing the longevity and carbon resistance of Ni-based catalysts.[5] Studies have shown that alloying nickel with iridium enhances the catalyst's resistance to carbon deposition, which is crucial for maintaining performance in high-temperature reactions. Additionally, it has been observed that supporting small metal clusters on larger particles can further increase resistance to coking compared to using either small clusters or large particles alone.[14,15] Incorporating Ir has been found to enhance the carbon resistance of these catalysts by raising the activation energy required for methane dissociation, thereby slowing down carbon deposition, especially under pressurized conditions.[16] This is particularly beneficial in preventing catalyst deactivation due to coke formation, a common challenge in DRM. Rhodium, another valuable addition, contributes by enhancing the reducibility of nickel, which is key to maintaining the catalyst's stability and performance during reactions.[12] This is particularly important in DRM, where the formation of synthesis gas with a desirable H_2/CO ratio is crucial for producing clean fuels and chemicals.[17] Rhodium also promotes the dissociative adsorption of oxygen, aiding in the gasification of carbon species and reducing the risk of coking.[12,18] This synergy between Rh and Ni not only boosts the overall reaction kinetics but also improves the structural integrity and thermal stability of the catalyst, making it more durable under the rigorous conditions of DRM.[17,18] Cobalt further complements these advantages by improving the catalyst's resistance to carbon deposition through its higher affinity for oxygen species, which facilitates the oxidation of carbon deposits.[19] The incorporation of cobalt improves the reducibility of nickel and facilitates the formation of Co−Ni alloys, which are recognized for their high reactivity in dry reforming of methane (DRM). Furthermore, the basic properties of hydrotalcite-derived catalysts, improved by cobalt incorporation, aid in the activation of CO_2, further contributing to the catalyst's resistance to coke formation.[20] These alloys, combined with cobalt's ability to improve metal−support interactions, result in catalysts with better dispersion of active metal particles, higher resistance to sintering, and improved overall catalytic performance.[21]

The incorporation of these group 9 elements into hydrotalcite-based catalysts also benefits from the unique properties of hydrotalcite, such as its inherent resistance to carbon formation and thermal sintering. The use of hydrotalcite as a precursor allows for the uniform distribution of metal particles and the development of catalysts with small crystal sizes and

https://doi.org/10.1021/acsomega.5c08293
ACS Omega XXXX, XXX, XXX−XXX

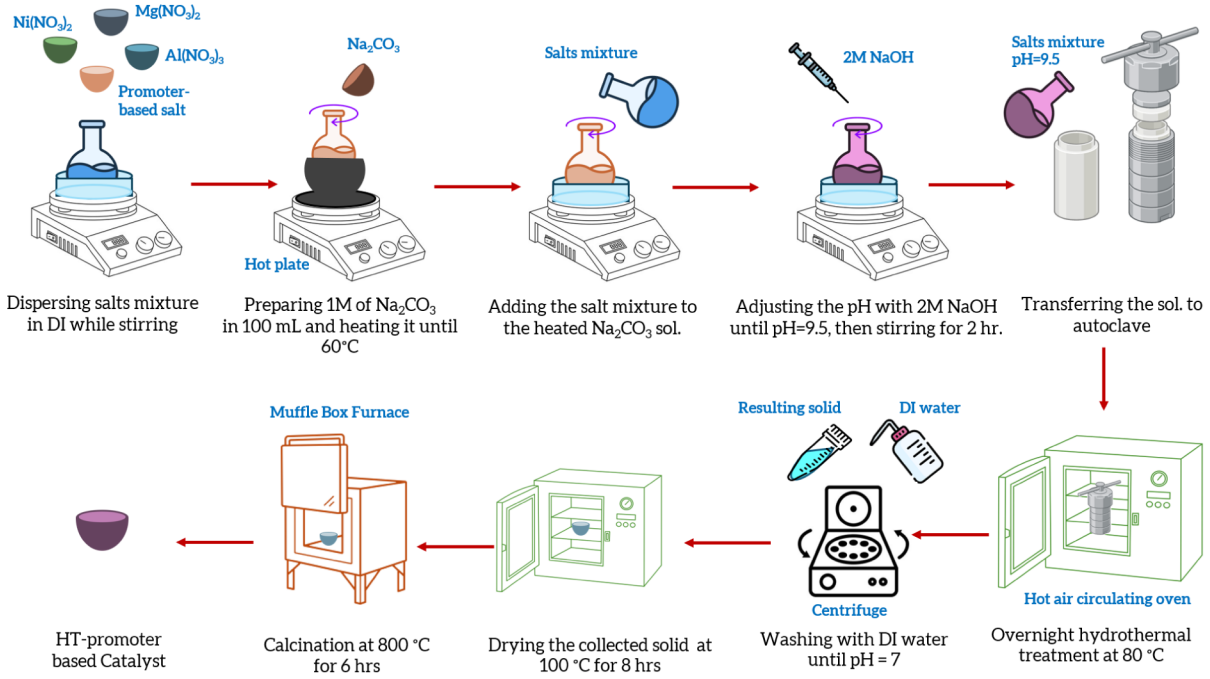

Figure 1. Schematic diagram of Ni-based HT catalyst synthesis by the coprecipitation method.

large specific surface areas, which are essential for efficient heterogeneous catalysis. Collectively, the strategic integration of Ir, Rh, and Co into these catalysts not only enhances their resistance to common deactivation pathways but also significantly improves their long-term stability and performance, making them highly suitable for industrial applications in which durability and efficiency are critical. In the recent literature, there are very few studies on the integration of these elements, especially Ir and Rh. Therefore, this study aims to systematically evaluate and compare the performance of hydrotalcite-derived Ni-based catalysts modified with small amounts of the group 9 elements.

2. METHODOLOGY

2.1. Materials. The following chemicals were used for catalyst synthesis: nickel(II) nitrate hexahydrate ($Ni(NO_3)_2 \cdot 6H_2O$, 98%, Alfa Aesar), magnesium nitrate hexahydrate ($Mg(NO_3)_2 \cdot 6H_2O$, 98%, Alfa Aesar), and aluminum nitrate nonahydrate ($Al(NO_3)_3 \cdot 9H_2O$, ≥98%, Fluka). Sodium carbonate (Na_2CO_3, ≥99%, Sigma-Aldrich) was employed as the precipitating agent. For metal promotion, rhodium(III) chloride hydrate ($RhCl_3 \cdot xH_2O$, 38.5−45.5% Rh, Alfa Aesar), cobalt(II) chloride anhydrous ($CoCl_2$, 99.7%, Alfa Aesar), and iridium(III) chloride hydrate ($IrCl_3 \cdot xH_2O$, reagent grade, Sigma-Aldrich) were utilized. All chemicals were used as received without further purification.

2.2. Catalyst Preparation. Ni-based hydrotalcite catalysts modified with Ir, Co, and Rh were prepared in a one-step coprecipitation method, as shown in Figure 1. Four catalysts were prepared for this study and are denoted as NiHT, NiHT-Ir, NiHT-Rh, and NiHT-Co. Nitrate salts of Mg, Ni, and Al were dissolved in 75 mL of DI water. The Mg/Al/Ni molar ratio was 2.5:1:0.212. For the catalysts modified with group 9 elements, $IrCl_3$, $RhCl_3$, and $CoCl_2$ salts were added to the mixture at 20% of the weight of Ni. A small aliquot of 1 M Na_2CO_3 (preheated to 60 °C) was first added to provide CO_3^{2-} for carbonate-LDH intercalation and solution buffering; 2 M NaOH was then added dropwise until a pH of 9.5 was obtained. This pH avoids $Al(OH)_3$ redissolution while favoring LDH nucleation. After 2 h of stirring, the solution was transferred to a Teflon-coated autoclave and kept overnight at 80 °C for hydrothermal treatment. The hydrothermally treated mixture was then washed and filtered using centrifugal filtration until a neutral pH was obtained. The collected solids were heated in a furnace at 100 °C for 8 h and calcined at 800 °C for 6 h in one step.

2.3. Catalyst Characterization. The experimental procedures for characterization techniques, including X-ray diffraction (XRD), scanning electron microscopy (SEM), transmission electron microscopy (TEM), X-ray photoelectron spectroscopy (XPS), N_2 physisorption, temperature-programmed reduction (H_2-TPR), temperature-programmed desorption (CO_2-TPD and NH_3-TPD), and thermogravimetric analysis (TGA), are provided in the Supporting Information.

2.4. Catalytic Evaluation. The catalytic activity of the prepared catalysts in the dry reforming of methane reaction was evaluated in a MicroEffi fixed-bed reactor with a 6 mm internal diameter and a 300 mm length. For every evaluation, 200 mg of catalyst was used. The catalyst underwent an in situ reduction in 5% H_2/Ar gas mixture for 60 min. The flow during this process was 100 mL/min at a temperature of 800 °C, followed by argon gas flow at a lower temperature of 750 °C. After that, a stoichiometric mixture of methane and carbon dioxide gases was introduced into the system at a rate of 50 mL/min for the DRM reaction. The performance of these catalysts was evaluated at a temperature of 750 °C for 20 h and at 30,000 $mL \cdot g_{cat}^{-1} \cdot h^{-1}$ gas hourly space velocity. The gaseous products—carbon monoxide and hydrogen—as well as unreacted methane and carbon dioxide, were analyzed using an in-line mass spectrometer. This evaluation aimed to determine methane and carbon dioxide conversions, hydrogen and carbon monoxide yields, and their molar ratio.

https://doi.org/10.1021/acsomega.5c08293
ACS Omega XXXX, XXX, XXX−XXX

2.5. DFT Calculations. All computational simulations were carried out employing the CP2K molecular dynamics software package,[22] utilizing the PBE exchange−correlation functional[23,24] alongside Grimme's D3 dispersion correction.[25] Valence electrons were described explicitly using a DZVP basis set with a plane-wave energy cutoff set at 500 Ry to truncate the basis. Core electrons were represented by GTH pseudopotentials.[22,26] An electronic temperature of 500 K was applied to properly account for the population of spin channels during the calculations.

Since our focus was on the molecular understanding of CO_2 and CH_4 adsorption processes on the LDH interface, we modeled our system using a single LDH layer, i.e., a two-dimensional (2D) slab interface with two vacuum/metal interfaces, starting from a previously optimized double-layered lamellar hydroxide (LDH) structure taken from the work of Coustel et al.[27]

All details of the system preparation are reported in the Supporting Information. Following a similar approach in the literature,[28,29] the adsorption energy for CO_2 or CH_4 on the different doped structures was then calculated as $E_{ads} = E_{compl} - (E_X + E_{sub})$, where E_{compl} is the energy of the total system containing the adsorbed species on the substrate and E_X and E_{sub} are the energies of the gas-phase (X = CO_2 or CH_4) and the catalyst substrate, respectively. All of the energies refer to the energies of the optimized structures, with and without the adsorbed molecule.

3. RESULTS AND DISCUSSION

3.1. Catalyst Characterization. The XRD patterns of the calcined samples, reported in Figure 2, indicate the typical peaks of MgO−NiO solids or $MgAl_2O_4$/$NiAl_2O_4$ spinels formed after the calcination of hydrotalcite.[12,20] The XRD results exhibit mixed oxides for all of the prepared catalysts due to the effect of calcination, resulting in the destruction of the hydrotalcite layered structure. The typical diffraction peaks of the MgO−NiO solid solution were observed at 2θ = 36.9, 43, 63, 75, and 79. Due to the similarity in the 2θ values for $MgAl_2O_4$ and $NiAl_2O_4$ spinels, differentiation between the two phases is challenging. Indeed, typical peaks for $MgAl_2O_4$ or $NiAl_2O_4$ spinels were observed at 2θ = 32, 36.5, 44.5, 59, and 65, which are generally favored by a high calcination temperature.[19,30] For NiHT-Ir, very weak diffraction peaks were observed for IrO_2, whereas no peaks attributable to cobalt or rhodium oxides were detected in NiHT-Co and NiHT-Rh, respectively. This could be due to the very low amounts of Ir, Rh, and Co used in the synthesis and is an indication of good dispersion of the active metals in the bulk, which can also be confirmed by TEM−EDX mapping presented in Figure 4. Moreover, studies by Tichit et al. confirm that in composite catalysts containing Ni, Al, Mg, and Co, the divalent cations of these elements belong to the same lattice, with Co^{2+} "diluting" the surface of Ni^{2+}.

Hence, the broadness of certain diffraction peaks comes from the overlapping of signals of close 2 theta values and similar intensities, attributed to a mixture of oxide phases, which makes it difficult to accurately interpret the XRD profile of such materials.[31−33]

The SEM images are presented in Figure 3. This analysis reveals a similar morphology for all the calcined catalysts, showing irregular small crystals attributed to the destruction of the layered double hydroxide structure after calcination and the formation of mixed oxides.

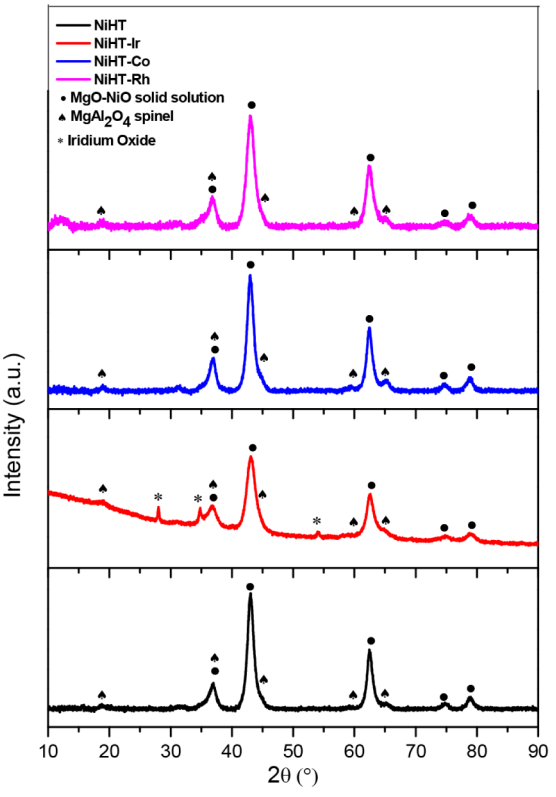

Figure 2. XRD characterization of calcined catalysts.

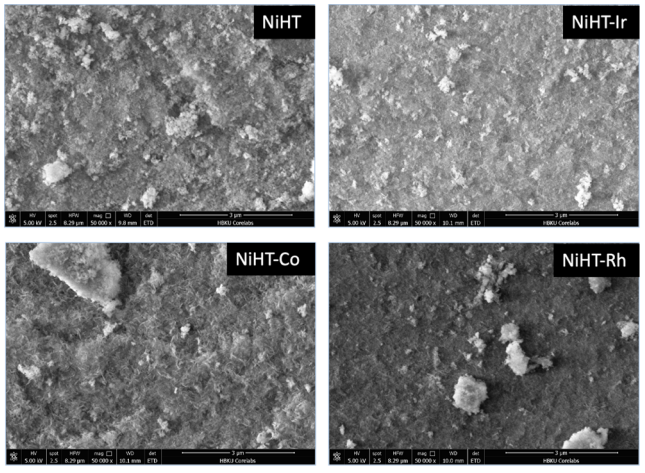

Figure 3. SEM images of calcined catalysts.

The TEM images of calcined hydrotalcite (NiHT and its modified forms: NiHT-Ir, NiHT-Co, and NiHT-Rh) in Figure 4 exhibit a highly dispersed nanosheet-like morphology. NiHT appears as thin, stacked, and exfoliated nanosheets with a somewhat wrinkled and porous structure, with noticeable aggregation suggesting structural collapse after calcination. The doped variants, NiHT-Ir, NiHT-Co, and NiHT-Rh, retain the nanosheet morphology but exhibit increased dispersion and possible fragmentation. The elemental mapping (EDX) images confirm the uniform distribution of Ni, Ir, Co, and Rh, indicating successful integration and homogeneous dispersion of these ions in the structure. Comparatively, the NiHT-Co

https://doi.org/10.1021/acsomega.5c08293
ACS Omega XXXX, XXX, XXX−XXX

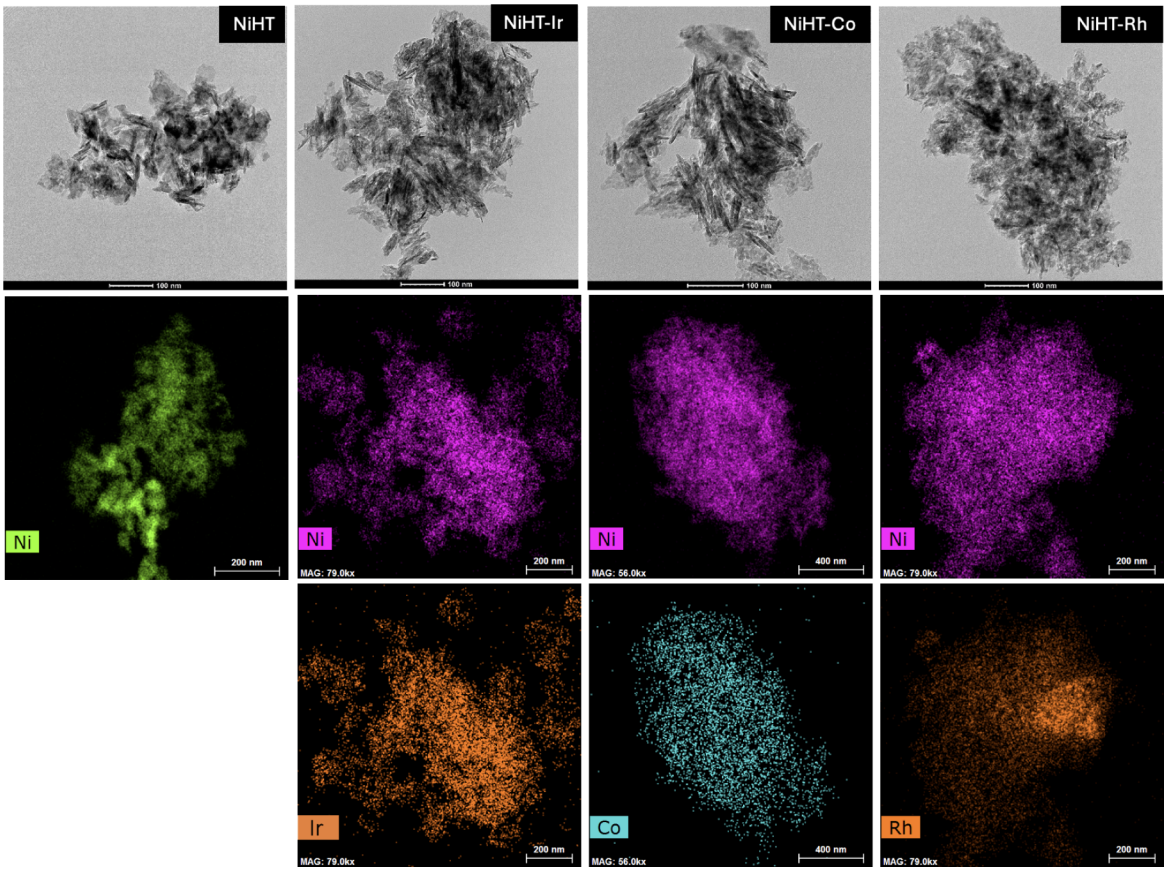

Figure 4. TEM−EDX images of calcined catalysts NiHT and its modified forms NiHT-Ir, NiHT-Co, and NiHT-Rh.

sample appears more fragmented and dispersed, while NiHT-Ir and NiHT-Rh exhibit denser aggregation of nanosheets, likely due to strong metal−support interactions. The presence of group 9 elements influences the textural properties and porosity, but overall, the calcined hydrotalcites maintain a layered and porous nanosheet-like morphology, with the degree of aggregation and dispersion varying depending on the ion.

TEM images were also utilized to determine the particle size and distribution of Ni and the added active metals (Ir, Co, and Rh). Image analysis was performed using dedicated processing software, revealing a broad normal distribution, with average particle sizes for Ni and the active metals ranging between 12 and 22 nm (Figures S3 and S6).

The X-ray photoelectron spectroscopy (XPS) spectra of the calcined hydrotalcite samples (NiHT, NiHT-Ir, NiHT-Co, and NiHT-Rh) provide insights into the electronic states and surface chemical compositions of the materials. Each spectrum corresponds to different elements present in the samples, with binding energy shifts indicating variations in oxidation states, metal−support interactions, and potential electronic modifications due to doping.

XPS characterization of the calcined fresh catalysts confirmed the presence of the principal elements associated with the hydrotalcite support, with distinct peaks observed for Ni 2p, Mg 1s, O 1s, C 1s, and Al 2p, as illustrated in Figure S1.

The O 1s spectra (Figure S1) provide valuable insights into the oxygen species present on the catalyst surface. The primary peak appears at ∼532 eV, which is characteristic of metal−oxygen bonding in oxides and hydroxides.[34] The consistency in the peak position across all samples suggests that the fundamental oxygen environment remains unchanged. However, minor intensity variations indicate slight differences in oxygen coordination due to interactions with the doped metals. The Mg 1s spectra, presented in Figure S1, exhibit a well-defined peak at ∼1304 eV, which is characteristic of Mg^{2+} in metal oxides. The consistent peak position and intensity across all samples indicate that the Mg species remain largely unaffected by the incorporation of Ir, Co, and Rh. The presence of Mg in the catalyst structure is expected as it originates from the hydrotalcite precursor, and it plays a crucial role in stabilizing the layered structure. The absence of significant binding energy shifts suggests that Mg does not directly interact with the doped metals but continues to contribute to the structural integrity of the material. In a similar fashion, the Al 2p region typically appears at ∼74−76 eV, corresponding to Al^{3+} in aluminum oxides and hydroxides. Since aluminum is an integral part of the hydrotalcite support, its consistent presence across all samples suggests that the structural framework remains intact despite the introduction of dopants. No significant shifts in binding energy are observed, indicating that Al does not participate in strong electronic interactions with Ir, Co, or Rh.

The Ni 2p spectra exhibit two main peaks: Ni 2p3/2 in the range of 850 to 860 eV and Ni 2p1/2 from 870 to 880 eV, with corresponding satellite peaks observed between 860−870 eV and 880−890 eV. The deconvolution of the Ni 2p spectrum indicates the coexistence of Ni^{2+} and Ni^{3+} oxidation states, with the Ni 2p3/2 peaks located at 856.6 and 858.5 eV, respectively. The calculated Ni^{2+} to Ni^{3+} ratio is approximately 1:0.3, suggesting a predominant Ni^{2+} state in the calcined catalysts.[35]

https://doi.org/10.1021/acsomega.5c08293
ACS Omega XXXX, XXX, XXX−XXX

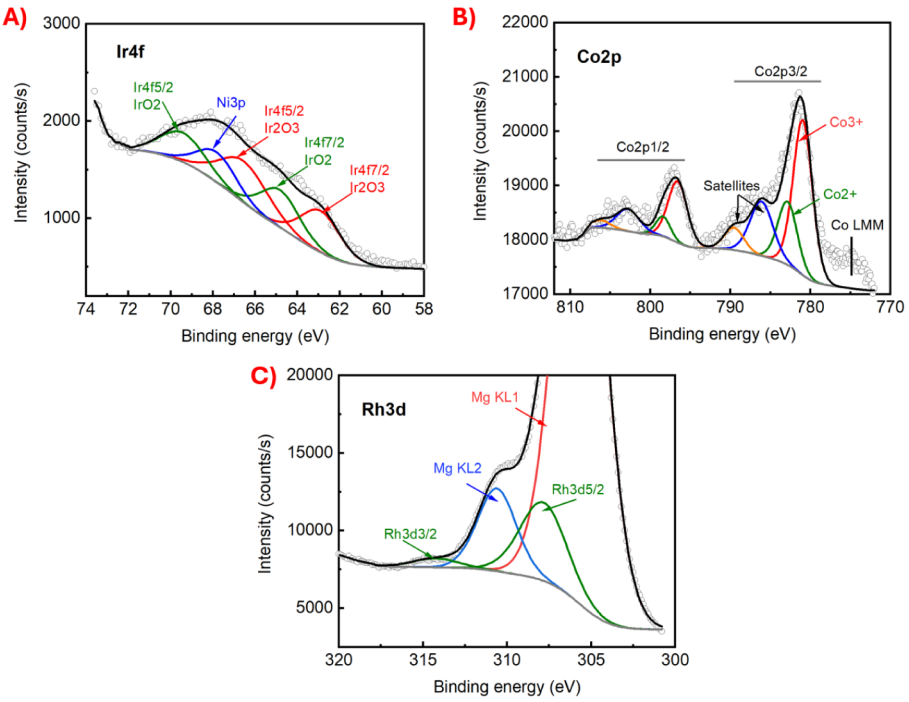

Figure 5. XPS analysis of calcined catalysts: (A) Ir 4f fitting for NiHT-Ir; (B) Co 2p fitting for NiHT-Co; (C) Rh 3d fitting for NiHT-Rh.

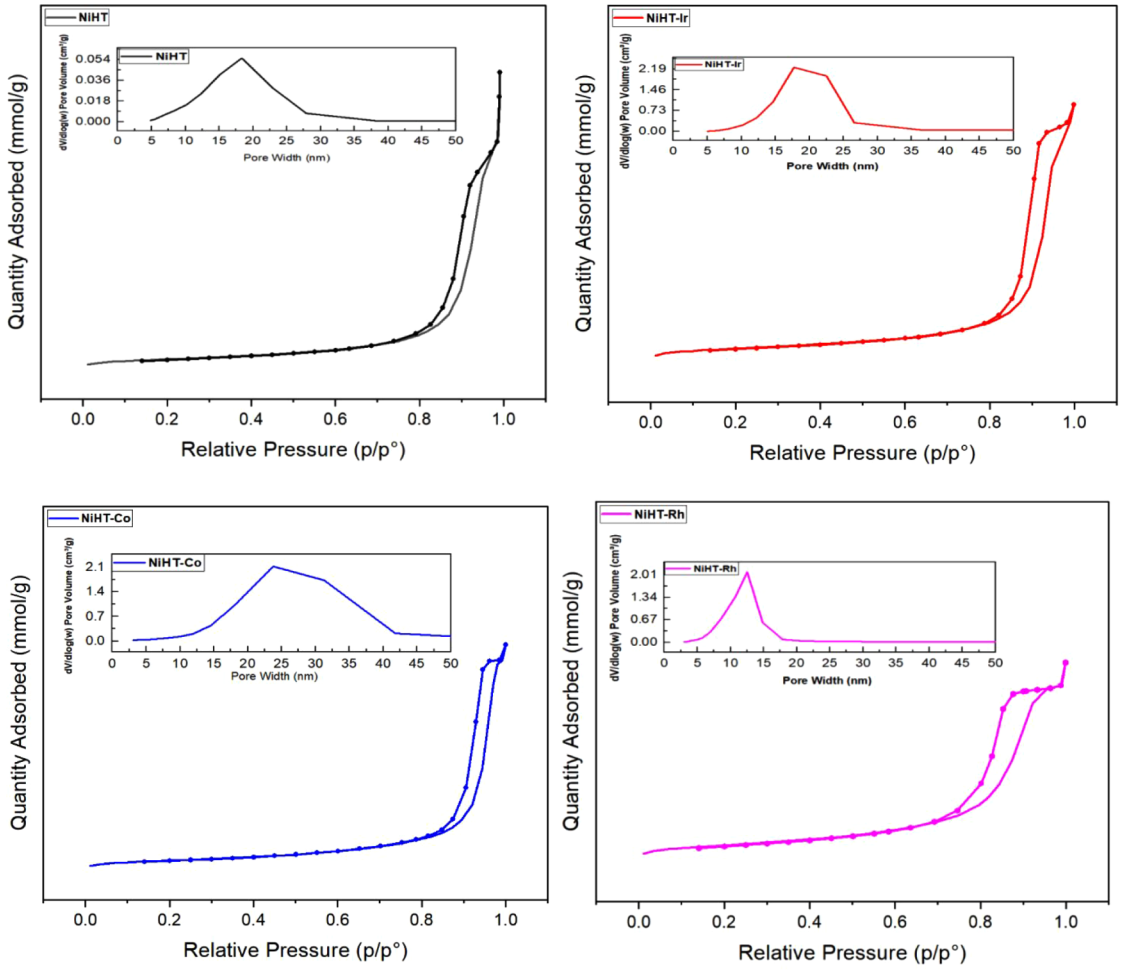

Figure 6. Nitrogen adsorption−desorption isotherms of the prepared catalysts.

https://doi.org/10.1021/acsomega.5c08293
ACS Omega XXXX, XXX, XXX−XXX

For the NiHT-Ir catalyst, the presence of iridium is confirmed by the detection of Ir 4f on the surface. The deconvoluted Ir 4f spectrum, presented in Figure 5A, identifies peaks corresponding to Ir_2O_3 and IrO_2, with the Ir 4f7/2 peaks located at 62.8 and 64.9 eV, respectively. These oxidation states of Ir are further supported by the XRD results, which confirm the formation of an iridium oxide species. Additionally, the Ni 3p peak is observed at approximately 68 eV, along with a Na 2s peak at 64 eV, indicating minor sodium contamination.

Similarly, the XPS analysis of the NiHT-Co sample reveals the presence of the primary support elements, along with the characteristic peaks for the group 9 metal Co 2p. As shown in Figure 5B, the Co 2p spectrum exhibits two main peaks: Co 2p3/2 at approximately 780 eV and Co 2p1/2 at 797 eV. The deconvolution of these peaks confirms the coexistence of Co^{2+} and Co^{3+} oxidation states, with Co 2p3/2 peaks identified at 780.9 eV (Co^{2+}) and 782.9 eV (Co^{3+}). Additionally, a peak observed at 775 eV is attributed to the Ni 2p LMM Auger signal, further confirming the interaction between Ni and Co in the catalyst structure.

In the case of the NiHT-Rh catalyst, the XPS spectrum indicates a relatively weak Rh 3d signal compared to that of NiHT, suggesting a lower surface concentration of rhodium. The Rh 3d region, ranging from 308 to 316 eV, is presented in Figure 5C. The deconvolution of the spectrum identifies the Rh 3d5/2 peak at 308.5 eV, which corresponds to a Rh−O bond structure, indicating the formation of a rhodium oxide species on the surface. However, the presence of a strong Mg Auger signal introduces spectral interference, making the precise quantification of Rh challenging. The presence of rhodium oxide is further supported by the XRD analysis, confirming the oxidation state of Rh in the calcined catalyst.

Overall, the XPS results indicate that the introduction of Ir, Co, and Rh influences the surface composition and electronic structure of Ni in the hydrotalcite-derived catalysts. The variations in binding energies and oxidation states suggest strong metal−support interactions, which could affect the catalytic performance of these materials.

3.2. Textural Properties. The nitrogen adsorption−desorption isotherms and corresponding pore size distributions of the calcined catalysts (NiHT, NiHT-Ir, NiHT-Co, and NiHT-Rh), shown in Figure 6, provide valuable information about their surface area, porosity, and overall textural characteristics. Based on IUPAC classification, all isotherms correspond to type V with H1 hysteresis loops, which are indicative of mesoporous structures typically ranging from 2 to 50 nm in diameter.[36−38] The BET surface areas and pore volumes, summarized in Table 1, reveal comparable surface areas across the four samples, with NiHT-Rh exhibiting the highest value and NiHT-Ir exhibiting the lowest. The pore size distribution (inset) reveals that the NiHT catalyst exhibits a peak at approximately 18 nm, with an average of 23 nm, indicating the formation of well-defined mesopores following the calcination of the hydrotalcite precursor. Similarly, the NiHT-Ir catalyst shows a broader distribution centered around 20 nm, suggesting a slightly smaller average pore size compared to NiHT. This difference may be attributed to the interaction between Ir species and the support, which could alter the pore structure and enhance mesoporosity. For the NiHT-Co catalyst, the adsorption isotherm displays a more pronounced hysteresis loop, and the pore size distribution exhibits a broad peak around 26 nm. This suggests that cobalt incorporation significantly modifies the pore structure, likely through the formation of Co oxide species that influence the pore walls and lead to an increase in average pore size. In contrast, the NiHT-Rh catalyst displays a sharp peak centered around 12 nm, indicative of the development of smaller mesopores relative to the other catalysts, possibly resulting from Rh oxide species blocking or partially occupying the larger pores.

Table 1. BET Surface Area, Pore Volume, and Pore Size Analysis of the Investigated Catalysts

Catalyst	BET Surface Area, S_{BET} [m^2/g]	Micropore area [m^2/g]	Total Pore Volume, V_t [cm^3/g]	Average pore size [nm]
NiHT	101.23	12.21	0.9926	23.32
NiHT-Ir	96.86	17.52	0.5860	17.29
NiHT-Co	98.72	11.45	0.7567	21.98
NiHT-Rh	108.77	9.58	0.4849	11.74

The H_2-TPR (temperature-programmed reduction) profiles of the calcined hydrotalcite-based catalysts (NiHT, NiHT-Ir, NiHT-Co, and NiHT-Rh) provide crucial insights into the reduction behavior, metal−support interactions, and the impact of additional metals on catalyst reducibility. The experiments were conducted to probe the reducibility of NiO species and their interaction with the Mg−Al oxide matrix, as well as to assess how Ir, Co, and Rh influence these properties.

All catalysts exhibit a major reduction band between ∼700 and 800 °C (Figure 7), which is attributed to Ni species

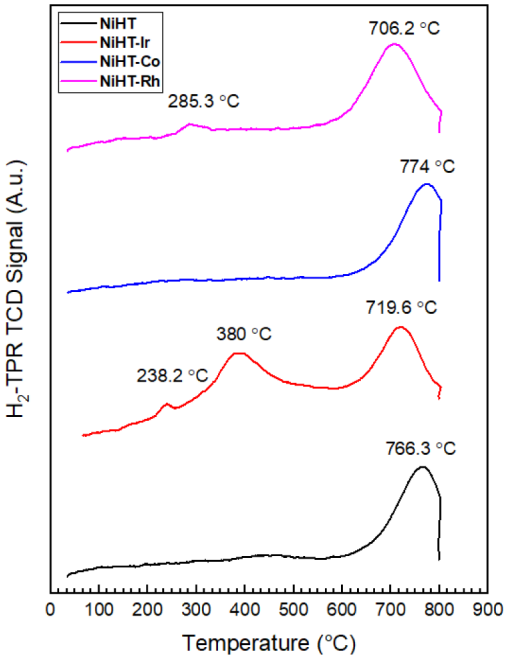

Figure 7. H_2-TPR results for calcined catalysts.

strongly coupled to the Mg−Al oxide, spinel-like environments formed upon calcination, that require elevated temperatures for reduction.[15] In NiHT, the principal peak at 766.3 °C is assigned to $Ni^{2+} \rightarrow Ni^0$ in strongly interacting NiO/Ni−support domains, consistent with a high degree of Ni incorporation within the Mg−Al matrix.

For NiHT-Ir, three features are observed at 238.2 °C, 380 °C, and 719.6 °C. We assign the 238.2 °C event to the

https://doi.org/10.1021/acsomega.5c08293
ACS Omega XXXX, XXX, XXX−XXX

Table 2. Results of H_2-TPR, Pulse Chemisorption, CO_2-TPD, and NH_3-TPD

	H_2 -TPR			H_2 -Pulse Chemisorption		CO_2 -TPD		NH_3 -TPD	
Catalysts	Peaks (°C)	Quantity (cm^3/g STP)	Ni Loading (%)	Ni Dispersion (%)	Metallic surface area (m^2/g metal)	Peaks (°C)	Quantity (cm^3/g STP)	Peaks (°C)	Quantity (cm^3/g STP)
NiHT	766.3	43.58	14.50	0.18	1.208	74.7, 382.7	13.18	115.8, 368.1	0.7270
NiHT-Ir	238.2, 380, 719.6	66.02	22.0	1.49	9.928	78.8, 357	40.45	119.5, 352.5	0.9034
NiHT-Co	774	48.92	16.30	1.30	8.634	83.8, 384	21.53	119.2, 358.4	0.9422
NiHT-Rh	285.3, 706.2	48.16	16.10	0.92	6.153	75.5, 368.6	21.87	119.9, 366.1	0.8639

reduction of Ir species ($IrO_x \rightarrow Ir^0$) that are readily reducible due to limited interaction with the support. The 380 °C peak is attributed to H_2-spillover-assisted reduction of nearby NiO (and/or a minor contribution from more weakly bound IrO_x), occurring slightly below the canonical ∼397 °C peak reported for unsupported NiO.[4,39,40] The main Ni-related band shifts to 719.6 °C, indicating that Ir promotes Ni reducibility, plausibly via hydrogen spillover from Ir sites.[41]

For NiHT-Co, a broad high-temperature peak at 774 °C is observed and assigned to $Ni^{2+} \rightarrow Ni^0$ in strongly interacting Ni−support domains. The slightly higher T_{max} than that of NiHT suggests either a marginally greater Ni−matrix coupling or the partial formation of mixed Ni−Co−oxide environments, which renders Ni reduction more difficult.

For NiHT-Rh, two peaks appear at 285.3 and 706.2 °C. We attribute the 285.3 °C feature to the reduction of Rh species ($RhO_x \rightarrow Rh^0$) together with spillover-assisted reduction of adjacent NiO. The main Ni-related peak at 706.2 °C lies below that of NiHT, evidencing that Rh, like Ir, facilitates NiO reduction via a spillover pathway.[42]

The absence of sub-400 °C reduction features in NiHT and NiHT-Co indicates a predominance of Ni that is integrated into the Mg−Al matrix and therefore requires higher temperatures to reduce. In contrast, NiHT-Ir and NiHT-Rh display low-temperature events (<∼380 °C) that arise from promoter reduction ($IrO_x/RhO_x \rightarrow Ir^0/Rh^0$) and H_2-spillover-assisted NiO reduction in their vicinity. These low-T processes increase the fraction of readily reducible Ni species available near the reaction temperature.

Ideally, after the 800 °C in situ activation used prior to catalysis (as described in Section 2.4), both low-T and high-T populations are reduced to Ni^0, but their roles differ: the promoter-assisted, readily reducible fraction correlates with higher initial activity, while the spinel-derived, strongly coupled fraction yields anchored Ni^0 nanoparticles that are sintering-resistant and thus govern stability during DRM. This perspective unifies the observed promotional trends: Ir/Rh introduces sub-400 °C features and shifts the principal Ni band to lower T (facilitated reducibility) while retaining the high-T component (anchored Ni). It also aligns with our postreaction characterization, where Ir/Rh-promoted catalysts exhibit the smallest Ni particle growth relative to NiHT and NiHT-Co (see Supporting Information). Low-temperature reducibility in Ir/Rh systems reflects promoter reduction and H_2 spillover (a kinetic effect), whereas sintering resistance is governed by structural pinning: Ni nucleates at Ir/Rh sites and from spinel-derived domains to form anchored Ni^0 ensembles, which suppress migration−coalescence; hence the smallest post-reaction Ni growth observed for Ir/Rh.

Finally, the broad high-temperature bands in NiHT and NiHT-Co are consistent with Ni^{2+} (and, where detected, Ni^{3+}) stabilized within periclase/spinel-like matrices, in agreement with XRD/XPS; overall reducibility follows the extent of Ni incorporation and metal−support coupling.[15,43] Note that the high-temperature bands in NiHT and NiHT-Co evidence strong oxide-state coupling; however, upon reduction at 800 °C, the breaking of Ni−O−(Al/Mg) bonds releases mobile Ni adatoms at T ≫ Tammann,[44] so in the absence of anchoring centers (Ir/Rh), the nucleation density is low, and Ni coarsens rapidly under DRM conditions, explaining the larger particle growth in NiHT and NiHT-Co (see Table 3).

To further assess the dispersion of Ni species, H_2 pulse chemisorption was performed (Table 2). The results indicate that Ni dispersion values range from 0.18% to 1.49%, with the highest Ni dispersion (1.49%) observed in NiHT-Ir. The incorporation of Ir promotes the formation of smaller NiO particles due to a dilution effect, as previously reported,[5] leading to the highest metallic surface area (9.928 m^2/g). Similarly, NiHT-Co also exhibited a high Ni dispersion (1.30%) and a corresponding metallic surface area of 8.634 m^2/g, suggesting that Co incorporation helps stabilize smaller NiO particles. The NiHT-Rh catalyst had a Ni dispersion of 0.92% with a metallic surface area of 6.153 m^2/g.

Conversely, the monometallic NiHT catalyst showed the lowest Ni dispersion and metallic surface area, which can be attributed to Ni particle aggregation. Recent studies suggest that higher Ni loading can lead to increased dispersion and metallic surface area in Ni−Mg−Al hydrotalcite catalysts,[12] but without an additional metal, Ni tends to aggregate, reducing its effectiveness in catalytic applications.

To examine the basicity of the prepared catalysts, CO_2-TPD experiments were employed. The peaks at lower temperatures below 150 °C generally indicate weak basic sites resulting from the interaction of Brønsted −OH groups with metal or alumina.[4] Peaks between 150 °C and 300 °C are ascribed to medium basic sites due to Lewis's acid−base sites and metal−O^{2-} pairs, while temperatures higher than 300 °C correspond to strong basic sites ascribed to isolated O^{2-} anions.[45]

As depicted in Figure 8, all of the catalysts exhibit two distinct CO_2 desorption peaks, confirming the presence of both weak and strong basic sites. However, the intensity and temperature of these peaks vary across different catalysts, suggesting differences in basic site distribution and strength.

The NiHT-Ir catalyst exhibits a higher intensity peak at 368.6 °C, indicating a higher concentration of strong basic sites compared to weak ones. This suggests that the incorporation of Ir enhances strong basicity, which can be attributed to the presence of IrO_2 species, as confirmed by XRD and XPS analysis. The ability of IrO_2 to modify the electronic environment of the support may increase the number of strong O^{2-} anions, leading to a higher desorption temperature. In contrast, the NiHT-Co and NiHT-Rh catalysts, as well as the monometallic NiHT, display more prominent low-temperature peaks (∼75−85 °C), indicative of a higher

https://doi.org/10.1021/acsomega.5c08293
ACS Omega XXXX, XXX, XXX−XXX

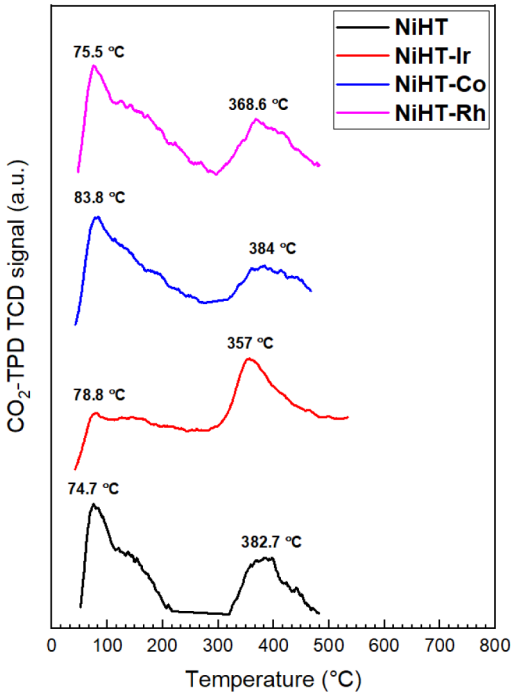

Figure 8. CO_2-TPD results of the calcined catalysts.

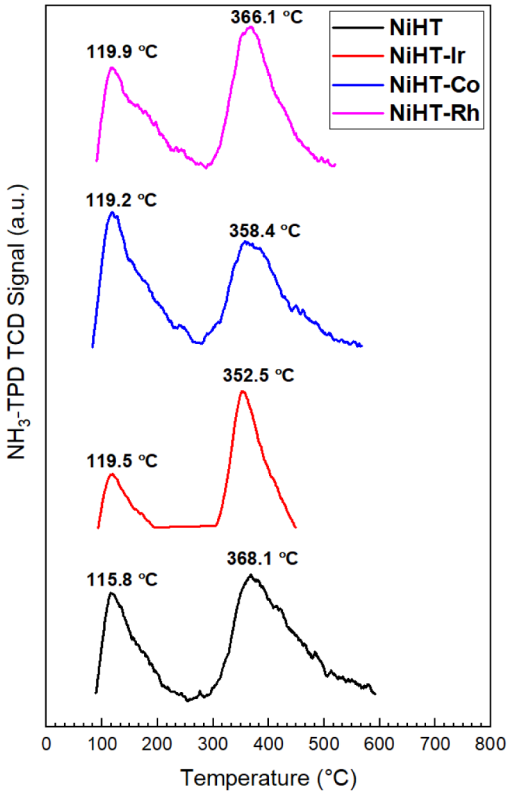

Figure 9. NH_3-TPD results of the calcined catalysts.

proportion of weak basic sites. This suggests that the basicity in these samples arises primarily from surface hydroxyl groups reacting with CO_2 to form bicarbonates.[45] The strong basic sites in NiHT-Co (~384 °C) and NiHT-Rh (~368.6 °C) are present but relatively less pronounced compared to NiHT-Ir, indicating that Co and Rh do not enhance basicity as significantly as Ir does. The monometallic NiHT catalyst exhibits the lowest basicity, with its strong basic peak appearing at 382.7 °C, but with lower intensity compared to the bimetallic samples. This suggests that without additional metals, the catalyst retains a lower concentration of strong O^{2-} anions, leading to weaker CO_2 adsorption. From a quantitative perspective, the CO_2-TPD results in Table 2 show that the total basic site density (as indicated by CO_2 desorption volume) is significantly enhanced upon Ir doping (40.45 cm^3/g STP), compared to the undoped NiHT (13.18 cm^3/g STP). This suggests an increased number of accessible basic sites, especially of medium and strong strength. Similarly, Co and Rh doped samples exhibit moderate increases in CO_2 uptake (~21−22 cm^3/g STP), indicating that these dopants also enhance basicity, albeit to a lesser extent than Ir. The enhanced CO_2 basic site concentration, exhibited by NiHT-Ir, correlates with the improved catalytic stability and coke resistance under the DRM conditions discussed in the coming sections.

The NH_3-TPD analysis was performed to evaluate the acidity of the prepared catalysts, with the results presented in Figure 9, where the NH_3 desorption peaks correspond to the strength and distribution of acid sites. All the catalysts exhibit two major NH_3 desorption peaks: low-temperature peaks (115−120 °C), which correspond to weak acid sites typically associated with physisorbed NH_3 molecules and Brønsted acid sites on hydroxyl groups from the Mg−Al mixed oxide support, and high-temperature peaks (352−370 °C), which correspond to medium-strength acid sites often attributed to Lewis acid sites associated with metal cations (Ni^{2+}, Ir^{3+}, Co^{2+}, Rh^{3+}) and strong metal−support interactions.

The presence of both weak and medium acid sites across all samples confirms that these catalysts maintain an amphoteric nature, balancing both acidic and basic functionalities, which is beneficial for bifunctional catalysis.

3.3. Adsorption Energy Calculations. To rationalize the observed differences in catalytic performance, particularly the superior performance of NiHT-Ir and NiHT-Rh, we performed DFT calculations to investigate the adsorption energies of DRM reactants (CH_4 and CO_2) on the various single-atom-doped LDH, as described in Section 2 and shown in Figure 10

The adsorption energies are reported in Table 3. CO_2 exhibits a higher adsorption energy (in absolute value) compared to CH_4 across all of the considered substrates. The presence of a group IX cocatalyst metal, i.e., Co, Rh, or Ir, enhances the adsorption of both CO_2 and CH_4 compared to the Ni-only system (LDH-Ni in Table 3). This effect is more pronounced for CO_2, with an increased adsorbate stability of 2.2 kcal/mol on LDH-Ni-Ir compared to LDH-Ni. For CH_4; however, the stability increment between double-metal-doped and Ni-only-doped systems is minimal, a fraction of kcal/mol. Regarding adsorption on the different double-doped substrates, i.e., LDH-Ni-Co, LDH-Ni-Rh, and LDH-Ni-Ir, we observed that the Ir-doped system exhibits the highest adsorption energies, indicating the greatest stability for the adsorbates, particularly for CO_2. However, the differences among the three cocatalyst metals are minimal, about 1 kcal/mol or less, especially in the case of CH_4.

The adsorption energy trends reported in Table 3 align with the optimized structures presented in Figure S2. For LDH-Ni-Rh and LDH-Ni-Ir, the adsorption geometries of CO_2 and

https://doi.org/10.1021/acsomega.5c08293
ACS Omega XXXX, XXX, XXX−XXX

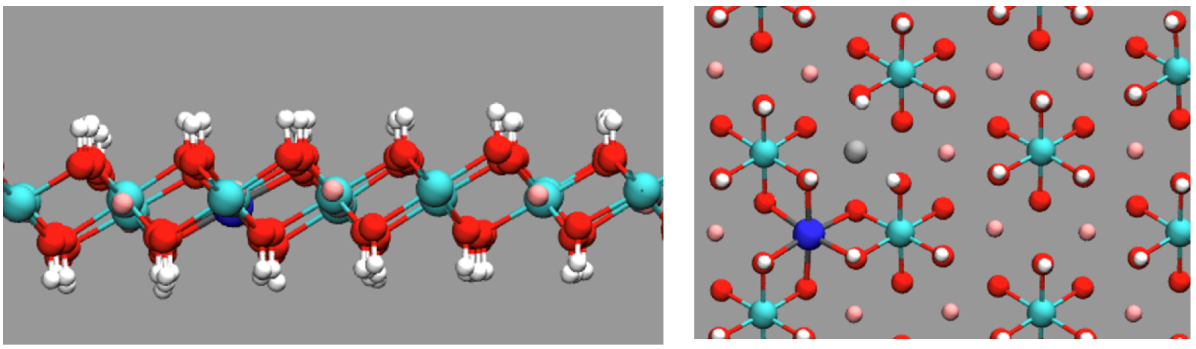

Figure 10. (a) Side view of the LDH layer; (b) top view of the LDH layer doped with Ni and Co. Color code: Ni (light gray), Co (blue), Al (cyan), H (white), O (red), and Mg (pink).

Table 3. Adsorption Energies for CO_2 and CH_4 on the Different Doped LDH Layers

Catalyst	E_{abs} CO_2 (kcal/mol)	E_{abs} CH_4 (kcal/mol)
LDH-Ni	−25.5	−21.5
LDH-Ni-Co	−26.2	−21.6
LDH-Ni-Rh	−26.3	−21.9
LDH-Ni-Ir	−27.7	−21.9

CH_4 are identical. Therefore, Figure S2 only displays the structures for Rh and Co as cocatalysts.

In summary, we observe an increased adsorption compared to bare LDH with Ni alone, particularly in the presence of cocatalysts, with the most notable effect seen for CO_2 and the Ir cocatalyst. However, the differences are minimal (also considering that experiments are at ∼750 °C, where thermal energy KBT ∼ 2 kcal/mol), and no significant structural changes are observed in Figure S2. Nevertheless, it is interesting to observe that the stronger CO_2 adsorption on NiHT-Ir (−27.7 kcal/mol) compared to NiHT (−25.5 kcal/mol) aligns well with experimental findings showing the increased number of basic sites and enhanced CO_2 activation observed in CO_2-TPD, both contributing to its higher coke resistance.

3.4. Catalytic Performance Evaluation. The catalytic performance and stability of the hydrotalcite-derived Ni-based catalysts were evaluated through the dry reforming of methane (DRM) at 750 °C for 20 h, using a gas hourly space velocity (GHSV) of 30,000 $mL \cdot g_{cat}^{-1} \cdot h^{-1}$. The reaction temperature was selected in view of the highly endothermic nature of DRM, which typically requires operation between 627 and 1000 °C under atmospheric pressure to approach thermodynamic equilibrium, while simultaneously reducing carbon deposition and ensuring catalyst stability.

As depicted in Figure 11, CO_2 conversion was consistently higher than CH_4 conversion for all catalysts tested. This behavior is attributed to the occurrence of the reverse water-gas shift (RWGS) reaction, which enhances CO formation and influences the evolution of the H_2/CO ratio over time.

Among the catalysts investigated, NiHT-Ir demonstrated the most outstanding performance, achieving the highest CH_4 and CO_2 conversions and maintaining a favorable H_2/CO ratio throughout the 20-h reaction. Its superior stability and coke resistance are linked to several critical factors, including improved Ni dispersion and a larger metallic surface area, as evidenced by H_2-pulse chemisorption results (Table 2), which increase the density of active sites for DRM.[46] Furthermore, the CO_2-TPD measurements indicated a higher concentration of strong basic sites, promoting efficient CO_2 adsorption and activation while limiting carbon accumulation. These synergistic effects account for the excellent durability and sustained catalytic activity exhibited by NiHT-Ir.

Similarly, the NiHT-Rh catalyst displayed excellent catalytic behavior, sustaining high CH_4 and CO_2 conversions and a

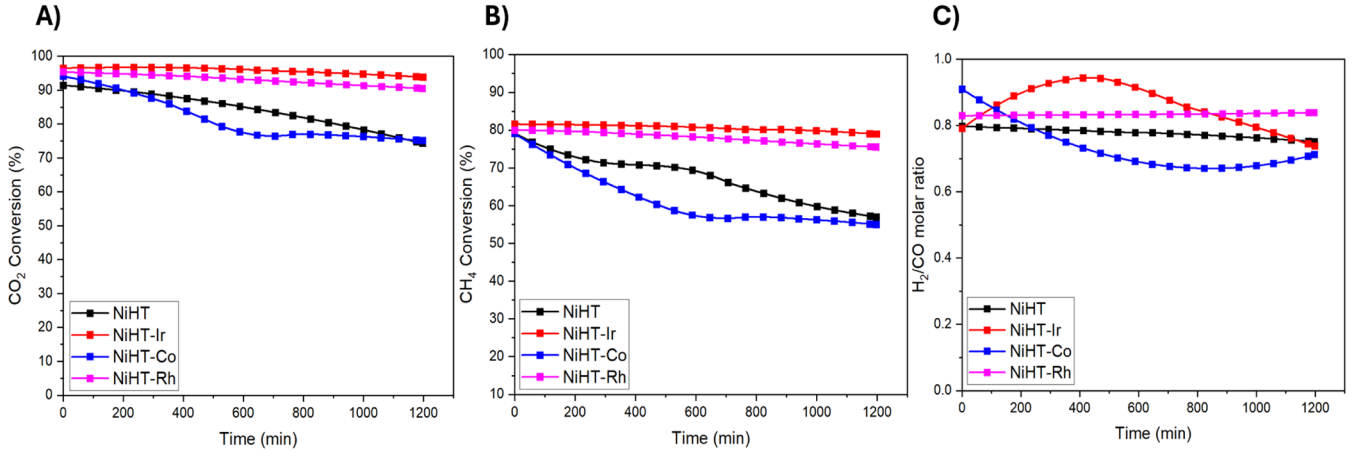

Figure 11. Catalytic performance of the catalysts investigated: (A) CO_2 conversion; (B) CH_4 conversion; (C) H_2/CO ratio.

https://doi.org/10.1021/acsomega.5c08293
ACS Omega XXXX, XXX, XXX−XXX

stable H_2/CO ratio over the reaction period. The enhanced coke resistance of NiHT-Rh is ascribed to the incorporation of rhodium, which is widely recognized for its ability to suppress carbon formation. Additionally, BET surface area analysis showed that NiHT-Rh maintained a relatively high surface area, contributing to better dispersion of Ni active sites, while H_2-TPR data confirmed robust metal−support interactions, further supporting high CH_4 activation efficiency and catalyst stability.

In contrast, NiHT-Co exhibited inferior performance compared with the Ir- and Rh-promoted catalysts. Although the initial CH_4 and CO_2 conversions were comparable to those observed for NiHT-Rh, the activity declined significantly with time, stabilizing at around 60% CH_4 and 75% CO_2 conversion within the first 10 h of reaction. This decrease in activity has been tentatively attributed to the slightly lower basicity, as evidenced by CO_2-TPD results, which suggest fewer strong basic sites available for CO_2 activation. Additionally, particle size analysis of the group 9 elements on the corresponding spent catalysts (Table S2 and Figure S6) revealed higher sintering of cobalt particles compared to iridium and rhodium.[47] Therefore, the loss of activity is likely linked to the reduced effectiveness of Co in maintaining Ni dispersion and inhibiting sintering under DRM conditions, contributing to the rapid deactivation of NiHT-Co.

For the monometallic NiHT catalyst, the conversion trends were similar to those of NiHT-Co, exhibiting gradual deactivation over time. As observed in Figure 11, both CO_2 and CH_4 conversions declined rapidly, which is a clear indication of catalyst deactivation due to carbon deposition. The rapid loss of stability, as further confirmed by the TGA results, suggests that NiHT is more prone to carbon accumulation and sintering, leading to a progressive reduction in catalytic activity. The lack of additional metals (Ir, Rh, or Co) results in a lower dispersion of active Ni species, making it more susceptible to sintering and coke formation.

The H_2/CO ratio (Figure 11c) was significantly influenced by the catalyst composition. NiHT-Ir exhibited the most stable and optimal H_2/CO ratio, remaining near 0.9, close to the stoichiometric DRM value of 1.0. The stability of the ratio suggests that NiHT-Ir effectively balances CH_4 and CO_2 activation, minimizing side reactions such as the reverse water-gas shift (RWGS) reaction.

Conversely, NiHT-Co displayed significant variation in the H_2/CO ratio over time, initially exhibiting a higher ratio due to preferential CH_4 decomposition, followed by a decline as CO_2 conversion decreased. This further confirms the lower CO_2 activation ability of NiHT-Co, leading to excess CH_4 decomposition and an imbalance in the H_2/CO ratio.

The NiHT-Rh catalyst maintained a stable H_2/CO ratio similar to that of NiHT-Ir, further supporting its high catalytic stability and coke resistance. In contrast, NiHT displayed the least stable H_2/CO ratio, further highlighting its tendency toward deactivation and instability during DRM.

The catalytic performance of Ni-based hydrotalcite-derived catalysts in DRM confirms that the incorporation of Ir and Rh significantly enhances both activity and stability, while Co negatively affects the long-term conversion efficiency. The NiHT-Ir catalyst exhibited the best performance, attributed to a combination of high nickel dispersion and metallic surface area, strong metal−support interactions, and enhanced basicity, which minimize carbon deposition.

NiHT-Rh also demonstrated high stability and coke resistance, making it a promising candidate for DRM applications. Indeed, Ir and Rh promote better Ni dispersion and inhibit sintering by forming solid solutions or surface alloys, as evidenced by the smaller Ni particle sizes (Figure S3) and higher metallic surface areas measured by TEM and chemisorption, respectively. This structural stabilization is further supported by TPR analysis, which shows that Ir and Rh facilitate NiO reduction at lower temperatures through hydrogen spillover, thereby enhancing the availability of active Ni^0 sites during DRM. Additionally, the presence of Ir and Rh modifies the electronic environment of the Ni and support, as revealed by XPS, contributing to altered adsorption energies for CH_4 and CO_2. DFT calculations confirm that Ir and Rh doping increases the strength of CO_2 adsorption, which correlates with the increased number of strong basic sites detected via CO_2-TPD. These basic sites play a crucial role in promoting the activation of CO_2 and scavenging surface carbon species, ultimately reducing coke formation.

On the other side, NiHT-Co and monometallic NiHT suffered from progressive deactivation, with NiHT-Co exhibiting lower CO_2 activation and NiHT showing the highest susceptibility to coking and sintering. In fact, although Co also enhances Ni dispersion and contributes to moderate basicity, it is less effective in suppressing sintering and carbon deposition over extended reaction periods.

Collectively, these findings highlight that the promotional effects of Ir and Rh are multifaceted, enhancing reducibility, improving dispersion, tuning adsorption properties, and increasing basicity, all of which contribute to improved DRM activity and resistance to deactivation.

3.5. Spent Catalyst Characterization. To evaluate coke deposition, metal sintering, and overall catalyst stability following 20 h of dry reforming of methane, the spent catalysts were analyzed using TGA, XPS, and TEM analyses. The corresponding results are illustrated in Figures 12, 13, and 14,

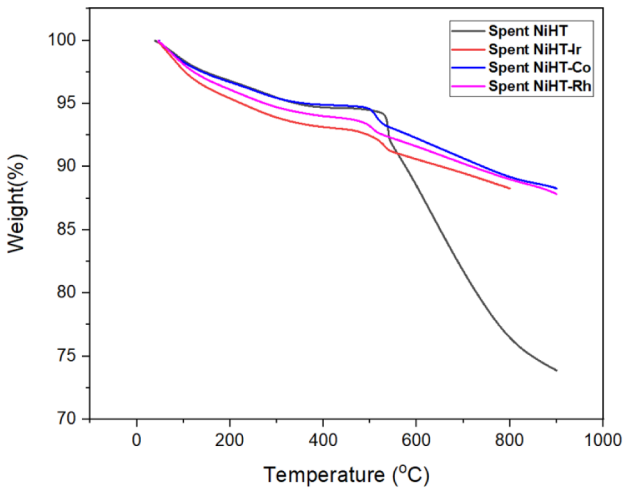

Figure 12. TGA results of the spent catalysts.

respectively. In addition, Table 4 summarizes the coke content (expressed as weight %) measured by TGA after reaction at 750 °C. These analyses offer valuable insights into the extent of carbon accumulation, the spatial distribution of active metal species, and the degree of nickel sintering, factors that critically influence catalyst longevity and performance.

https://doi.org/10.1021/acsomega.5c08293
ACS Omega XXXX, XXX, XXX−XXX

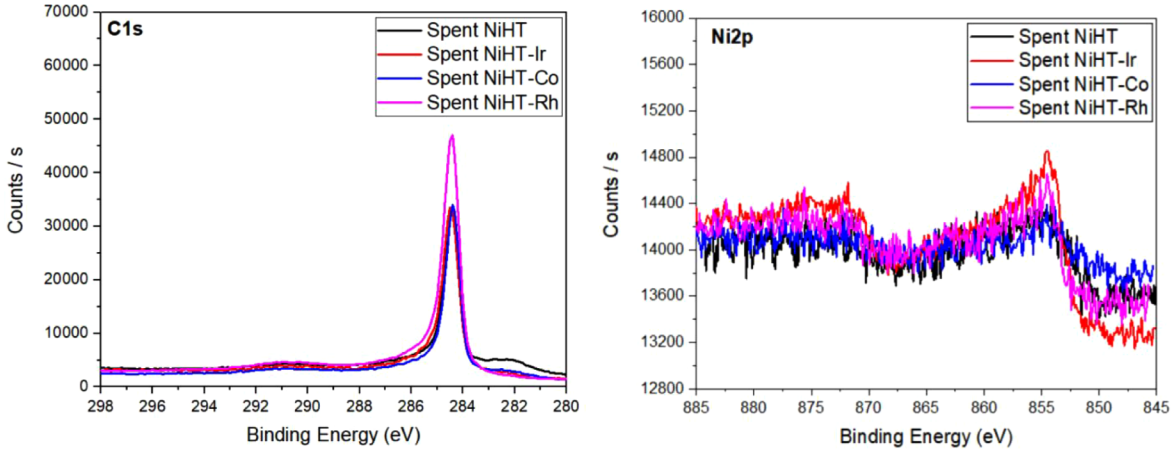

Figure 13. XPS analysis of the spent catalysts: (left) C 1s; (right) Ni 2p.

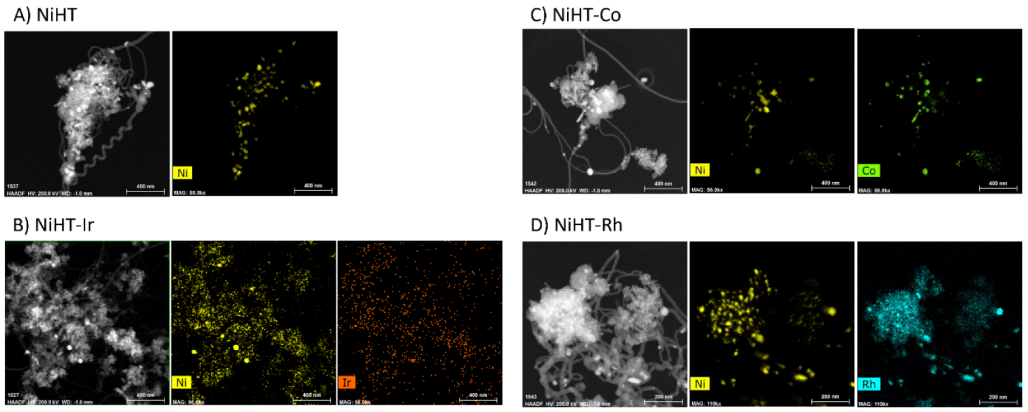

Figure 14. TEM-EDX images of spent catalysts: (A) NiHT and its modified forms; (B) NiHT-Ir, (C) NiHT-Co, and (D) NiHT-Rh.

Table 4. Catalytic Conversions, Coke Formation, and Nickel Sintering

Catalyst	CH_4 Initial Conversion (% @ 10 min)	CH_4 Final Conversion (% @ 1200 min)	CO_2 Initial Conversion (% @ 10 min)	CO_2 Final Conversion (% @ 1200 min)	Coke Formation (%)	Ni Sintering (nm)
NiHT	79.40	60.13	91.43	74.64	17	+32.12
NiHT-Ir	81.64	80.63	96.36	95.78	4.5	+7.88
NiHT-Co	79.21	54.13	93.21	76.39	5.5	+42.48
NiHT-Rh	79.39	74.34	95.04	90.68	6	+15.65

For all bimetallic catalysts, TGA profiles revealed a modest weight loss occurring between 450 and 550 °C, indicative of the dominant morphology and reactivity of the deposited carbon species. The temperature range of mass loss is commonly associated with the nature of coke, whereas the intensity of the weight change correlates with its quantity.[48] Among the tested samples, the spent NiHT catalyst showed the highest coke accumulation (approximately 17 wt %), suggesting significant carbon buildup during the reaction. In contrast, the introduction of secondary metals markedly suppressed coke formation, underscoring their beneficial role in enhancing resistance to carbon-induced deactivation.

The XPS C 1s spectra (Figure 13) confirm the presence of sp^2 hybridized carbon, with binding energies ranging from 284.65 to 284.84 eV, characteristic of graphitic carbon. The formation of graphitic coke was further validated by TEM images, which revealed filamentous carbon structures, including multiwall carbon nanotubes (MWCNTs).

Additionally, the XPS analysis of the spent catalysts revealed significant changes in the Ni 2p profile compared with the fresh catalysts. The Ni 2p signals were notably weaker, indicating a considerable reduction in the Ni availability on the surface. This could be attributed to carbon encapsulation, which prevents the exposure of Ni sites, or to metal sintering, which reduces the active surface area. The active metal species Ir, Co, and Rh also exhibited different stability behaviors after the reaction.

The TEM images of the spent catalysts (Figure 14) highlight the tip-growth formation of carbon nanotubes, where Ni particles are encapsulated in carbon layers. This structure confirms the formation of graphitic coke around active Ni sites, a well-known coking mechanism in DRM, where Ni particles catalyze carbon deposition during methane dissociation. The particle size distribution analysis (Table S1 and Figure S4) confirms that Ni sintering was most severe in NiHT-Co, leading to a significant loss of catalytic stability. The Ni particle size increased substantially after the reaction with NiHT-Co

https://doi.org/10.1021/acsomega.5c08293
ACS Omega XXXX, XXX, XXX−XXX

exhibiting the highest degree of sintering at +42.48 nm, contributing to its poor long-term performance. In contrast, NiHT-Ir displayed the least sintering at +7.88 nm, correlated with its superior stability and minimal coke formation.

The overall catalytic performance of the spent catalysts, as presented in Table 4, shows that NiHT-Ir maintained the highest CH_4 and CO_2 conversion with minimal decline over time. NiHT-Rh also exhibited good stability, while NiHT-Co suffered from severe sintering and decreased activity. The monometallic NiHT catalyst performed the worst, showing rapid deactivation due to excessive coke formation and sintering, as evidenced by the high weight loss in TGA analysis.

In a fashion similar to the sintering analysis of nickel particles, the sintering of the group 9 metals (Figure S6 and Table S2) has been estimated by particle size distribution. Such analysis revealed that the sintering follows the order Rh < Ir < Co, helping in understanding how the cocatalyst can also be affected by the reaction conditions.

Postreaction characterization of the spent catalyst confirms that the incorporation of Ir, Co, and Rh significantly improves coke resistance and Ni stability, with NiHT-Ir exhibiting the most stable performance over 20 h of DRM. The low coke deposition and minimal Ni sintering in NiHT-Ir suggest that Ir plays a crucial role in preserving catalyst activity. Meanwhile, NiHT-Co suffered from extensive sintering, making it the least stable catalyst in DRM.

The XPS characterization of the spent catalysts (Figure S5) provides valuable insight into the chemical transformations occurring during the dry reforming of methane. In the case of the Co-promoted catalyst, the Co 2p spectrum reveals a partial reduction of Co^{3+} and Co^{2+} species to metallic Co^0, as indicated by a shift in binding energy to lower values and the appearance of a Co^0 peak near 778 eV. This change, along with a reduction in overall peak intensity, suggests that Co may have undergone sintering or been partially encapsulated by carbon during the reaction, consistent with the observed decline in catalytic performance. For the Ir-promoted catalyst, the Ir 4f spectrum remains largely unchanged before and after the reaction, with the IrO_2 and Ir_2O_3 signals still clearly visible. This indicates that Ir remains in its oxidized states and is chemically stable under the reaction conditions, which aligns with the superior performance and minimal deactivation observed for NiHT-Ir. In contrast, the Rh 3d region shows a slight shift toward lower binding energy after the reaction, pointing to a partial reduction of Rh^{3+} to Rh^0. Despite some reduction, the Rh species largely retain their surface presence, and no significant loss in peak resolution is observed. These spectral shifts reflect the differing stability and reactivity of the group 9 elements during DRM, with Ir showing the greatest chemical resilience, Rh remaining moderately stable, and Co being the most prone to structural and electronic changes under reaction conditions.

The multitechnique approach using TGA, TEM, and XPS provides strong evidence that metal–support interactions play a key role in mitigating catalyst deactivation, reinforcing the importance of cocatalysts in improving long-term catalyst durability.

4. CONCLUSION

The catalytic performance and stability of hydrotalcite-derived Ni-based catalysts in DRM were significantly influenced by the incorporation of group 9 metals. The addition of Ir, Co, and Rh altered the physicochemical properties of the catalysts, affecting their reducibility, metal–support interactions, and coke resistance. Among the tested catalysts, NiHT-Ir exhibited the best performance, maintaining high CH_4 and CO_2 conversions and minimal deactivation over 20 h. The superior stability of NiHT-Ir is attributed to strong metal–support interactions, high Ni dispersion, and a greater number of basic sites, which reduced carbon deposition. NiHT-Rh also demonstrated excellent catalytic stability, benefiting from strong metal–support interactions and a high surface area. In contrast, NiHT-Co suffered from extensive Ni sintering, leading to a significant decrease in activity over time. The monometallic NiHT catalyst exhibited the worst performance, with rapid deactivation due to excessive coke formation and metal sintering. Computational results further corroborated the enhanced adsorption behavior of CO_2 on Ir- and Rh-modified surfaces, supporting their superior experimental performance.

The spent catalyst characterization confirmed that Ir and Rh effectively suppressed coke formation and minimized Ni sintering, while Co promoted metal aggregation, reducing the catalytic stability. The combination of advanced characterization techniques and catalytic evaluation highlights the role of dopants in enhancing the catalyst performance. This study demonstrates that Ir and Rh are highly effective promoters for improving the durability and efficiency of Ni-based DRM catalysts, making them promising candidates for industrial applications. Future studies will address longer-term deactivation behavior.

■ ASSOCIATED CONTENT

Supporting Information

The Supporting Information is available free of charge at https://pubs.acs.org/doi/10.1021/acsomega.5c08293.

XPS spectra and elemental analysis (fresh and spent catalysts); BET surface area and pore size distribution; DFT model structures and adsorption energies; Ni and promoter particle size distributions (Tables S1–S2); and complementary characterization data (Figures S1–S6) (PDF)

■ AUTHOR INFORMATION

Corresponding Authors

Alessandro Sinopoli − *Qatar Environment and Energy Research Institute, Hamad Bin Khalifa University, Doha, Qatar; Department of Chemical, Biological, Pharmaceutical and Environmental Sciences, University of Messina, Messina 98166, Italy;* orcid.org/0000-0001-7993-4268; Email: alessandro.sinopoli@unime.it

Tareq Al-Ansari − *Qatar Environment and Energy Research Institute, Hamad Bin Khalifa University, Doha, Qatar; Division of Sustainable Development, College of Science and Engineering, Hamad Bin Khalifa University, Doha, Qatar;* orcid.org/0000-0002-2932-8240; Email: talansari@hbku.edu.qa

Authors

Sumia Manzoor − *Qatar Environment and Energy Research Institute, Hamad Bin Khalifa University, Doha, Qatar; Division of Sustainable Development, College of Science and Engineering, Hamad Bin Khalifa University, Doha, Qatar; University of Leeds, Leeds, England LS2 9JT, U.K.*

Ahmed Abotaleb − *Qatar Environment and Energy Research Institute, Hamad Bin Khalifa University, Doha, Qatar*

https://doi.org/10.1021/acsomega.5c08293
ACS Omega XXXX, XXX, XXX−XXX

Nada Abounahia − *Qatar Environment and Energy Research Institute, Hamad Bin Khalifa University, Doha, Qatar*
Yongfeng Tong − *Qatar Environment and Energy Research Institute, Hamad Bin Khalifa University, Doha, Qatar;* orcid.org/0000-0002-0029-5289
Ivan Gladich − *Qatar Environment and Energy Research Institute, Hamad Bin Khalifa University, Doha, Qatar;* orcid.org/0000-0003-0929-3439
Abdraman Moussa − *Ministry of Environment and Climate Change, The Hazardous Chemical & Waste Department, Doha, Qatar*
Mohammed Alshamari − *Ministry of Environment and Climate Change, The Hazardous Chemical & Waste Department, Doha, Qatar*
Abdulrahman Altay − *Ministry of Environment and Climate Change, The Hazardous Chemical & Waste Department, Doha, Qatar*

Complete contact information is available at: https://pubs.acs.org/10.1021/acsomega.5c08293

Author Contributions

#S.M. and A.A. equally contributed.

Notes

During the preparation of this work, the authors used ChatGPT (OpenAI, 2024 version) to assist with language polishing and to improve the clarity and consistency of the scientific text. After using this tool, the authors thoroughly reviewed and edited the content as needed and took full responsibility for the content of the publication.
The authors declare no competing financial interest.

■ ACKNOWLEDGMENTS

The authors gratefully acknowledge the financial support provided by the Ministry of Environment and Climate Change (MOECC, Grant No. ENV-3-2023) and the Qatar National Research Fund (QRDI, Grant No. GSRA 10-L-2-0611-23112). Additional internal funding and institutional support were generously provided by the Qatar Environment and Energy Research Institute (QEERI), part of Hamad Bin Khalifa University (HBKU), a member of Qatar Foundation. The authors also thank Dr. Akshath Shetty, Mr. Janarthanan Ponraj, Mr. Mujaheed Pasha, Mr. Abdulaziz Al-Emadi, and Mr. Omar El Hassan (Core Laboratories at HBKU) for their assistance with material characterization. The findings presented in this publication are solely the responsibility of the authors. Dr. Ivan Gladich extends his appreciation to Dr. Romain Coustel and Dr. Erwan André for sharing the initial double-layered lamellar hydroxide (LDH) structure referenced in ref 27. The authors further acknowledge the Research Computing group at Texas A&M University at Qatar—funded by Qatar Foundation—for access to high-performance computing (HPC) resources and services, as well as the use of QEERI's HPC infrastructure under Project No. HPC-P21003.

■ REFERENCES

(1) Pier, F.; Trude, S.; Kyle, A.; William, C.; Jean-Louis, D.; David, F.; Lunt, D.; Thorsten, M.; Palmer, M.; Masahiro, W.*Chapter 7: The Earth's Energy Budget, Climate Feedbacks and Climate Sensitivity*Climate Change2021132
(2) Hussien, A.; Polychronopoulou, K. A review on the different aspects and challenges of the dry reforming of methane (DRM) reaction. *Nanomaterials* **2022**, *12*, 3400.
(3) Nguyen, D. L.; Tran, A. V.; Vo, D.-V. N.; Nguyen, H. T.; Rajamohan, N.; Trinh, T. H.; Nguyen, T. L.; Le, Q. V.; Nguyen, T. M. Methane dry reforming: A catalyst challenge awaits. *J. Ind. Eng. Chem.* **2024**, *140*, 169−189.
(4) Chatla, A.; Abu-Rub, F.; Prakash, A. V.; Ibrahim, G.; Elbashir, N. O. Highly stable and coke-resistant Zn-modified Ni-Mg-Al hydrotalcite derived catalyst for dry reforming of methane: Synergistic effect of Ni and Zn. *Fuel* **2022**, *308*, 122042.
(5) Huang, Y.; Li, X.; Zhang, Q.; Vinokurov, V. A.; Huang, W. Enhanced carbon tolerance of hydrotalcite-derived Ni-Ir/Mg (Al) O catalysts in dry reforming of methane under elevated pressures. *Fuel Process. Technol.* **2022**, *237*, 107446.
(6) Alhassan, A. M.; Hussain, I.; Taialla, O. A.; Awad, M. M.; Tanimu, A.; Alhooshani, K.; Ganiyu, S. A. Advances in catalytic dry reforming of methane (DRM): Emerging trends, current challenges, and future perspectives. *J. Cleaner Prod.* **2023**, *423*, 138638.
(7) Xu, Y.; Du, X.; Shi, L.; Chen, T.; Wan, H.; Wang, P.; Wei, S.; Yao, B.; Zhu, J.; Song, M. Improved performance of Ni/Al2O3 catalyst deriving from the hydrotalcite precursor synthesized on Al2O3 support for dry reforming of methane. *Int. J. Hydrogen Energy* **2021**, *46* (27), 14301−14310.
(8) Duan, X.; Pan, J.; Yang, X.; Wan, C.; Lin, X.; Li, D.; Jiang, L. Nickel−cobalt bimetallic catalysts prepared from hydrotalcite-like compounds for dry reforming of methane. *Int. J. Hydrogen Energy* **2022**, *47* (58), 24358−24373.
(9) Fan, G.; Li, F.; Evans, D. G.; Duan, X. Catalytic applications of layered double hydroxides: recent advances and perspectives. *Chem. Soc. Rev.* **2014**, *43* (20), 7040−7066.
(10) Rosset, M.; Féris, L. A.; Perez-Lopez, O. W. Biogas dry reforming over Ni-M-Al (M= K, Na and Li) layered double hydroxide-derived catalysts. *Catal. Today* **2021**, *381*, 96−107.
(11) Yuan, B.; Zhu, T.; Han, Y.; Zhang, X.; Wang, M.; Li, C. Deactivation Mechanism and Anti-Deactivation Measures of Metal Catalyst in the Dry Reforming of Methane: A Review. *Atmosphere* **2023**, *14* (5), 770.
(12) Berg, H. *The promotional effect of Ca, Mg, and Rh on the activity of Ni-based catalysts from hydrotalcite precursor for dry reforming of methane*; University of Stavanger: Norway, 2018.
(13) Gennequin, C.; Safariamin, M.; Siffert, S.; Aboukaïs, A.; Abi-Aad, E. CO2 reforming of CH4 over Co−Mg−Al mixed oxides prepared via hydrotalcite like precursors. *Catal. Today* **2011**, *176* (1), 139−143.
(14) Dagle, V. L.; Dagle, R.; Kovarik, L.; Genc, A.; Wang, Y.-G.; Bowden, M.; Wan, H.; Flake, M.; Glezakou, V.-A.; King, D. L.; et al. Steam reforming of hydrocarbons from biomass-derived syngas over MgAl2O4-supported transition metals and bimetallic IrNi catalysts. *Appl. Catal., B* **2016**, *184*, 142−152.
(15) Ahn, K.; Lee, J.-H.; Kim, H.; Kim, J. Enhanced carbon tolerance of Ir alloyed Ni-Based metal for methane partial oxidation. *Heliyon* **2018**, *4* (6), No. e00652.
(16) Liu, Z.; Gao, F.; Zhu, Y.-A.; Liu, Z.; Zhu, K.; Zhou, X. Bi-reforming of methane with steam and CO 2 under pressurized conditions on a durable Ir−Ni/MgAl 2 O 4 catalyst. *Chem. Commun.* **2020**, *56* (88), 13536−13539.
(17) Li, N.; Shen, C.; Tan, P.; Zuo, Z.; Huang, W. Effect of phase transformation on the stability of Ni-Mg-Al Catalyst For Dry Reforming Of Methane. *Indian J. Chem. A* **2015**, *54*, 1198−1205.
(18) Li, P.; Yu, F.; Altaf, N.; Zhu, M.; Li, J.; Dai, B.; Wang, Q. Two-dimensional layered double hydroxides for reactions of methanation and methane reforming in C1 chemistry. *Materials* **2018**, *11* (2), 221.
(19) Tanios, C.; Bsaibes, S.; Gennequin, C.; Labaki, M.; Cazier, F.; Billet, S.; Tidahy, H. L.; Nsouli, B.; Aboukaïs, A.; Abi-Aad, E. Syngas production by the CO2 reforming of CH4 over Ni−Co−Mg−Al catalysts obtained from hydrotalcite precursors. *Int. J. Hydrogen Energy* **2017**, *42* (17), 12818−12828.
(20) González, A. R.; Asencios, Y. J.; Assaf, E. M.; Assaf, J. M. Dry reforming of methane on Ni−Mg−Al nano-spheroid oxide catalysts prepared by the sol−gel method from hydrotalcite-like precursors. *Appl. Surf. Sci.* **2013**, *280*, 876−887.

(21) Abu-Rub, F. *Catalyst Synthesis & Characterization for Dry Reforming of Methane: Synthesis of Ni-based Hydrotalcite Catalyst by Impregnation Method*; LYRASIS, 2020.
(22) Hutter, J.; Iannuzzi, M.; Schiffmann, F.; VandeVondele, J. cp2k: atomistic simulations of condensed matter systems. *Wiley Interdiscip. Rev.: Comput. Mol. Sci.* **2014**, *4* (1), 15−25.
(23) Perdew, J. P.; Ruzsinszky, A.; Csonka, G. I.; Vydrov, O. A.; Scuseria, G. E.; Constantin, L. A.; Zhou, X.; Burke, K. Restoring the Density-Gradient Expansion for Exchange in Solids and Surfaces. *Phys. Rev. Lett.* **2008**, *100* (13), 136406.
(24) Perdew, J. P.; Burke, K.; Ernzerhof, M. Generalized Gradient Approximation Made Simple. *Phys. Rev. Lett.* **1996**, *77* (18), 3865−3868.
(25) Grimme, S.; Antony, J.; Ehrlich, S.; Krieg, H. A consistent and accurate ab initio parametrization of density functional dispersion correction (DFT-D) for the 94 elements H-Pu. *J. Chem. Phys.* **2010**, *132* (15), 154104.
(26) Goedecker, S.; Teter, M.; Hutter, J. Separable dual-space Gaussian pseudopotentials. *Phys. Rev. B* **1996**, *54* (3), 1703−1710.
(27) Coustel, R.; Boucly, A.; André, E.; Di Bitetto, A.; Bournel, F.; Gallet, J.-J.; Rochet, F.; Carteret, C. NAP-XPS Probes the Electronic Structure of the Mg−Al−Cl Layered Double Hydroxide upon Controlled Hydration. *J. Phys. Chem. C* **2023**, *127* (8), 4144−4153.
(28) Gladich, I.; Lin, C.; Sinopoli, A.; Francisco, J. S. Uptake and hydration of sulfur dioxide on dry and wet hydroxylated silica surfaces: a computational study. *Phys. Chem. Chem. Phys.* **2021**, *24* (1), 172−179.
(29) Liu, Z.; Sinopoli, A.; Francisco, J. S.; Gladich, I. Water-Catalyzed Formation of Reactive Oxygen Species from NO2 on a Weakly Hydrated Calcite Surface. *J. Am. Chem. Soc.* **2024**, *146* (26), 17898−17907.
(30) Zhang, J.; Wang, H.; Dalai, A. K. Development of stable bimetallic catalysts for carbon dioxide reforming of methane. *J. Catal.* **2007**, *249* (2), 300−310.
(31) Coq, B.; Tichit, D.; Ribet, S. Co/Ni/Mg/Al layered double hydroxides as precursors of catalysts for the hydrogenation of nitriles: hydrogenation of acetonitrile. *J. Catal.* **2000**, *189* (1), 117−128.
(32) Tichit, D.; Medina, F.; Coq, B.; Dutartre, R. Activation under oxidizing and reducing atmospheres of Ni-containing layered double hydroxides. *Appl. Catal., A* **1997**, *159* (1−2), 241−258.
(33) Zhu, F. L.; Meng, Y. S. Preparation and characterization of NiO nanowires via single-phase precipitation. *Adv. Mater. Res.* **2013**, *668*, 331−334.
(34) Dupin, J.-C.; Gonbeau, D.; Vinatier, P.; Levasseur, A. Systematic XPS studies of metal oxides, hydroxides and peroxides. *Phys. Chem. Chem. Phys.* **2000**, *2* (6), 1319−1324.
(35) Zhang, W.; Shen, H.; Yin, M.; Lu, L.; Xu, B.; Li, D. Heterostructure Silicon Solar Cells with Enhanced Power Conversion Efficiency Based on Si x/Ni3+ Self-Doped NiO x Passivating Contact. *ACS Omega* **2022**, *7* (19), 16494−16501.
(36) Thommes, M.; Kaneko, K.; Neimark, A. V.; Olivier, J. P.; Rodriguez-Reinoso, F.; Rouquerol, J.; Sing, K. S. Physisorption of gases, with special reference to the evaluation of surface area and pore size distribution(IUPAC Technical Report). *Pure Appl. Chem.* **2015**, *87* (9−10), 1051−1069.
(37) Inaba, M.; Murase, R.; Takeshita, T.; Yano, K.; Kosaka, S.; Takahashi, N.; Isomura, N.; Oh-Ishi, K.; Yoshimune, W.; Tsuchiya, K.; et al. Synthesis of a Mesoporous SnO2 Catalyst Support and the Effect of Its Pore Size on the Performance of Polymer Electrolyte Fuel Cells. *ACS Appl. Mater. Interfaces* **2024**, *16* (8), 10295−10306.
(38) Wang, G.; Zhao, W.; Mansoor, M.; Liu, Y.; Wang, X.; Zhang, K.; Xiao, C.; Liu, Q.; Mao, L.; Wang, M.; et al. Recent progress in using mesoporous carbon materials as catalyst support for proton exchange membrane fuel cells. *Nanomaterials* **2023**, *13* (21), 2818.
(39) García-Sancho, C.; Guil-López, R.; Pascual, L.; Maireles-Torres, P.; Navarro, R.; Fierro, J. Optimization of nickel loading of mixed oxide catalyst ex-hydrotalcite for H2 production by methane decomposition. *Appl. Catal., A* **2017**, *548*, 71−82.
(40) Song, J. H.; Park, D. C.; You, Y.-W.; Chang, T. S.; Heo, I.; Kim, D. H. Lean NO x reduction by CO at low temperature over bimetallic IrRu/Al 2 O 3 catalysts with different Ir: Ru ratios. *Catal. Sci. Technol.* **2020**, *10* (7), 2120−2136.
(41) Shen, H.; Li, H.; Yang, Z.; Li, C. Magic of hydrogen spillover: Understanding and application. *Green Energy Environ.* **2022**, *7* (6), 1161−1198.
(42) Li, M.; Yin, W.; Pan, J.; Zhu, Y.; Sun, N.; Zhang, X.; Wan, Y.; Luo, Z.; Yi, L.; Wang, L. Hydrogen spillover as a promising strategy for boosting heterogeneous catalysis and hydrogen storage. *Chem. Eng. J.* **2023**, *471*, 144691.
(43) Nieva, M. A.; Villaverde, M. M.; Monzón, A.; Garetto, T. F.; Marchi, A. J. Steam-methane reforming at low temperature on nickel-based catalysts. *Chem. Eng. J.* **2014**, *235*, 158−166.
(44) Lif, J.; Odenbrand, I.; Skoglundh, M. Sintering of alumina-supported nickel particles under amination conditions: Support effects. *Appl. Catal., A* **2007**, *317* (1), 62−69.
(45) Abotaleb, A.; Abounahia, N.; Makeen, S.; Ponraj, J.; Al Yarabah, M.; Ferella, F.; Sinopoli, A. Assessing the recyclability of spent fluid catalytic cracking catalyst for sustainable dry reforming of methane. *Fuel* **2024**, *373*, 132356.
(46) Yuan, X.; Li, B.; Wang, X.; Li, B. Synthesis gas production by dry reforming of methane over Neodymium-modified hydrotalcite-derived nickel catalysts. *Fuel Process. Technol.* **2022**, *227*, 107104.
(47) Claeys, M.; Dry, M. E.; van Steen, E.; van Berge, P. J.; Booyens, S.; Crous, R.; van Helden, P.; Labuschagne, J.; Moodley, D. J.; Saib, A. M. Impact of Process Conditions on the Sintering Behavior of an Alumina-Supported Cobalt Fischer−Tropsch Catalyst Studied with an in Situ Magnetometer. *ACS Catal.* **2015**, *5* (2), 841−852.
(48) Cherbański, R.; Kotkowski, T.; Molga, E. Thermogravimetric analysis of coking during dry reforming of methane. *Int. J. Hydrogen Energy* **2023**, *48* (20), 7346−7360.

https://doi.org/10.1021/acsomega.5c08293
ACS Omega XXXX, XXX, XXX−XXX